JOURNAL OF SPACECRAFT AND ROCKETS
Vol. 39, No. 2, March–April 2002

Ionospheric Specification and Forecast Modeling

Robert W. Schunk,* Ludger Scherliess,† and Jan J. Sojka‡
Utah State University, Logan, Utah 84322-4405

The ionosphere is a highly dynamic medium that exhibits weather disturbances at all latitudes, longitudes, and altitudes. Unfortunately, the weather disturbances can have adverse effects on numerous civilian and military systems/operations, and consequently, a major effort has been devoted to developing ionospheric specification and forecast models. Over the years, a wide range of models have been developed, including empirical, parameterized, numerical, tomographic, and physics-based data assimilation models. The status of the various modeling approaches is briefly reviewed. The review covers the philosophy underlying the approaches and the strengths and limitations of the approaches. In each case, a representative example is given to show the attributes of the approach. The review should be useful to practitioners who are affected by the ionosphere, and it should serve as a benchmark against which future progress can be measured.

Nomenclature

$F_{10.7}$	=	10.7-cm solar flux, $WHz^{-1}m^{-2}$
f_0E	=	E-region critical frequency, MHz
f_0F_2	=	F_2-region critical frequency, MHz
h_mE	=	height of E-region density peak, km
h_mF_2	=	height of F_2-region density peak, km
K_p	=	3-h magnetic activity index
N_e	=	electron density, cm^{-3}
N_mE	=	peak electron density in E region, cm^{-3}
N_mF_2	=	peak electron density in F_2 region, cm^{-3}
R	=	sunspot number
R_E	=	Earth's radius, 6371 km

Introduction

THE ionosphere was discovered shortly after Marconi's experiments in 1901 involving trans-Atlantic radio waves. Since that time, the ionosphere has been studied extensively with the aid of balloons, rockets, satellites, and a wide range of ground-based instruments (ionosondes, all-sky cameras, magnetometers, incoherent scatter radars, and numerous optical instruments). In addition, there have been literally hundreds of model studies based on a wide range of model types, including empirical, physical, and data assimilation models. Because of the experimental and theoretical studies, it is now well known that the ionosphere displays an appreciable variation with altitude, latitude, longitude, universal time, solar cycle, season, and geomagnetic activity.

The variation of the ionosphere with altitude is shown in Fig. 1. Note that the electron density profile exhibits a layered structure, with distinct D, E, F_1, and F_2 regions. In the D and E regions, chemical processes determine the density structure, molecular ions dominate, and N_2, O_2, and O are the most abundant neutral species. Additionally, in the D region (60–100 km), there are both positive and negative ions, water cluster ions, and three-body chemical reactions. In the E region (100–150 km), the basic chemical reactions are less complicated, and the major ions are NO^+, O_2^+, and N_2^+. In the F_1 region (150–250 km), ion–atom interchange and transport processes start to become important, and in the F_2 region the ionization maximum occurs as a result of a balance between plasma transport and chemical loss processes. In these regions, the atomic species (O^+ and O) dominate. The topside ionosphere is generally defined to be the region above the F region peak, whereas the protonosphere is the region where the lighter atomic ions (H^+ and He^+) dominate. The peak electron densities in the E and F regions are designated by N_mE and N_mF_2, respectively, whereas the corresponding peak heights are designated by h_mE and h_mF_2.

The large variability of the ionosphere results from the couplings, time delays, and feedback mechanisms that are inherent in the ionosphere–thermosphere system, as well as from the effects of solar, interplanetary, magnetospheric, and mesospheric processes. The various processes act to define both a background ionospheric state (climatology) and a disturbed state (weather). The ionospheric features that are associated with the background state are different in the different latitudinal domains. At high latitudes, the primary climatological features include a tongue of ionization in the polar cap, a polar hole in winter, enhanced densities in the auroral oval, an electron density trough equatorward of the nocturnal auroral oval, and elevated dayside densities. At midlatitudes, the climatology is dominated by a relatively smooth latitude–longitude variation of both the dayside and nightside densities, with a gradual transition of high dayside to low nightside densities across the terminator. Finally, at low latitudes, the predominant climatological feature is the Appleton anomaly, which is a term used to describe the ionization crests that are located at about 10 deg on both sides of the magnetic equator. At the present time, the various climatological features have been clearly identified, as has their variation with season, solar cycle, and geomagnetic activity.

Superimposed on the background ionosphere is a wide range of weather disturbances, which are due to numerous processes, including changes in the interplanetary magnetic field, geomagnetic storms and substorms, upward propagating tides and gravity waves from the lower atmosphere, and plasma instabilities.[1] The weather disturbances, in turn, can have detrimental effects on a variety of important human activities and systems. The weather disturbances can affect over-the-horizon radars, hf communications, surveying and navigation systems that use global positioning system (GPS) satellites, surveillance, satellite lifetimes, satellite tracking, spacecraft charging, power grids, pipelines, and the Federal Aviation Administration's wide-area augmentation system.[2–7]

In an attempt to mitigate the adverse effects of the ionosphere on military and civilian systems, specification and forecast models are being used both to correct for ionospheric effects and to predict future adverse conditions. A wide range of ionospheric models is currently being used, including empirical, parameterized, numerical, tomographic, and physics-based data assimilation models. The purpose of this paper is to briefly review the various modeling approaches and to provide sufficient references for the interested reader to delve into more detail. The paper should be useful to practitioners

Received 27 February 2001; revision received 5 July 2001; accepted for publication 7 July 2001.

*Director, Center for Atmospheric and Space Sciences; schunk@cc.usu.edu. Member AIAA.
†Postdoctoral Fellow, Center for Atmospheric and Space Sciences.
‡Assistant Director, Center for Atmospheric and Space Sciences.

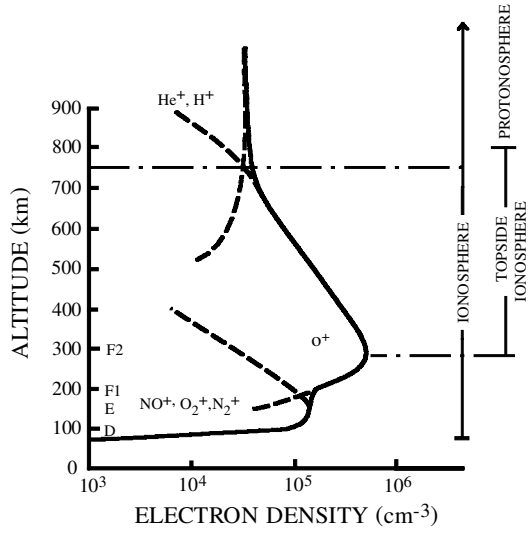

Fig. 1 Typical ion density profiles for the daytime midlatitude ionosphere showing the D, E, F_1, and F_2 regions.[1]

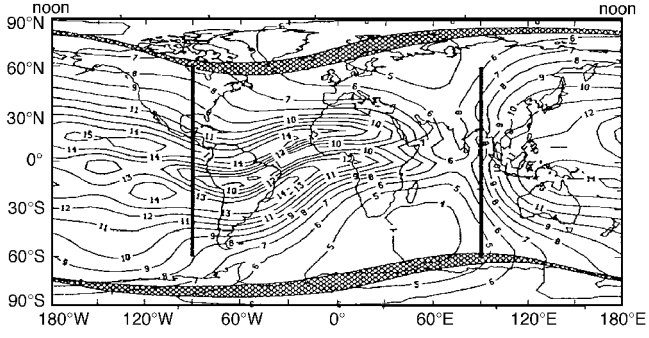

Fig. 2 Contours of f_0F_2 (MHz) from the IRI model for solar maximum (R = 190), September equinox and 0 UT (Ref. 10).

who are affected by the ionosphere, and it should serve as a benchmark against which future progress can be measured.

Empirical Models

Empirical models of the ionosphere have been available since the early 1970s,[8] and they are still being used for a variety of purposes. Empirical models are based on measurements. Before the models are constructed, data are typically collected over an extended period of time via remote (ionosondes, topside sounders, and incoherent scatter radars) or in situ (rockets and satellites) techniques. The data are synthesized, binned with the aid of appropriate indices, and then fitted with either analytical expressions or orthogonal functions. Because of this approach, the empirical models represent average, not instantaneous, conditions, and therefore, they describe the climatology of the system. Nevertheless, empirical ionospheric models are still used for specification and forecasting purposes. The empirical models are also used in a hybrid fashion to assist in the assimilation of real-time measurements into Kalman filter models.

The most comprehensive empirical model of the ionosphere is the International Reference Ionosphere (IRI), which is continually being updated by a community of international scientists.[9] The IRI provides information on the global distribution of the electron density, the ion composition, and the ion and electron temperatures. The information is obtained by specifying the date, time, position, and solar activity level (sunspot number), as well as the ionospheric parameters desired. The electron densities obtained from the IRI are monthly medians. Also, because of the data coverage, the IRI is more reliable at midlatitudes than in other domains, and the most reliable parameter is the peak electron density N_mF_2.

A representative global distribution of $f_0F_2[\sim(N_mF_2)^{1/2}]$ obtained from the IRI is shown in Fig. 2, where contours of f_0F_2 are displayed for solar maximum, September equinox, and universal time (UT) = 0 h (Ref. 10). Also shown are representative auroral ovals (shaded regions) and the sunrise/sunset terminators (vertical bars). The IRI displays many of the well-known features of the global N_mF_2 distribution. At low latitudes, the Appleton anomaly is clearly evident, as is the magnetic control of this feature. The two ionization crests form in the afternoon, one on each side of the magnetic equator, and they persist well into the night. At midlatitudes, the ionosphere exhibits a strong diurnal variation, with the highest densities in the afternoon and the lowest in the early morning hours. At high latitudes, the IRI yields a fairly uniform N_mF_2 distribution, which is an artifact of the model. The high-latitude ionosphere is typically very structured, but this structure is not reproduced by the IRI primarily because of the lack of measurements and the complexity of the structure.

Parameterized Models

Parameterized models are similar to empirical models in that they are based on orthogonal function fits to data. For empirical models, the data are measurements, whereas for parameterized models, the data are numerical outputs from physics-based ionospheric models. Typically, the physics-based numerical models provide a wealth of information about ionospheric behavior. The numerical models yield ion and electron densities, temperatures, and flow velocities as a function of altitude, latitude, longitude, and UT. In addition, simulations can be conducted for a wide range of geophysical conditions, including different solar cycle, seasonal, and magnetic activity levels. Over the years, it has been shown that nearly all of the known ionospheric features can be reproduced in numerical simulations, including plasma patches, auroral and boundary blobs, tongues of ionization, polar holes, ionization troughs, and the equatorial ionization crests. However, the physics-based models are not user friendly and generally require an excessive amount of CPU time. Therefore, it is unlikely that engineers and the general scientific community will ever have access to these models. Nevertheless, the output of the physical-based ionospheric models may be useful to the general community. In an effort to disseminate the information obtained from physics-based numerical models, the output is parameterized by fitting the output with orthogonal functions, and then a user-friendly interface is typically added so that the numerical data can be readily accessed.

A parameterized ionospheric model that is currently undergoing extensive validation is the parameterized real-time ionospheric specification model (PRISM).[11] PRISM contains two elements, including a parameterized ionospheric model (PIM) and a real-time adjustment (RTA) algorithm that incorporates real-time measurements. PIM is a global model of ionospheric climatology that is based on both numerical and empirical models. The ionospheric parameters are obtained from PIM by specifying a few inputs [altitude, latitude, longitude, UT, solar activity $F_{10.7}$, magnetic activity K_p, and the direction of the interplanetary magnetic field (IMF)]. The RTA algorithm starts from the PIM climatology and then adjusts it so that it is consistent with real-time measurements, and the net result is PRISM's real-time specification of the ionosphere. Currently, PRISM is capable of ingesting several measured parameters that pertain to the electron density profile, including f_0F_2, h_mF_2, f_0E, h_mE, vertical total electron content (TEC), and in situ electron densities measured along satellite orbits. The RTA algorithm is designed so that PRISM matches the real-time measurements at the locations where the measurements were made and then relaxes to the PIM climatology as one moves away from the measurement locations. The RTA algorithm will allow the real-time data to affect PRISM's output over a horizontal distance of about 2200 km away from the measurement locations.[12]

An extensive testing program for PRISM has recently been initiated using several data types, including ground-based GPS-TEC, ionosonde, and satellite data.[12–14] A simple example from one of these tests shows how PRISM works.[12] The test involved vertical TEC data obtained from a partial orbit of the TOPEX satellite. The particular orbit segment occurred on 18 April 1993, between 2138 and 2309 UT, when the satellite was in the geographic latitude range of from 25°N to 75°S. Figure 3 shows the vertical TEC measured by TOPEX along the orbit segment (solid curve). Also shown is the TEC variation along the orbit segment predicted by PRISM climatology (dashed curve). The dotted curve is PRISM TEC along the orbit

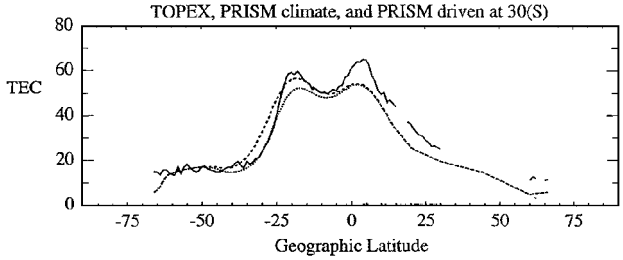

Fig. 3 TEC vs geographic latitude along a single TOPEX orbit.[12]

segment when the TEC measured by TOPEX at −30° latitude is used as a real-time input to PRISM. The RTA algorithm in PRISM adjusts PRISM's TEC to match the measurement at −30° latitude, and then the adjustment is reduced at distances away from the −30° location. By +5° and −50°, PRISM relaxes back to climatology. (The dotted and dashed curves agree.) Relative to climatology, the RTA algorithm with only one real-time data point improves the PRISM prediction at locations near the measurement but can actually yield worse predictions at other locations. This degradation in the predictions occurs because the climatology in the region where the RTA has an influence yields TEC values both above and below the measured TEC. Therefore, a decrease in the TEC climatology at one location (−30°) to match a measurement shifts the climatology curve downward in the RTA influence domain, and this downshift results in larger discrepancies at other locations (near the anomaly peak at −20°). The basic problem is that the shape of the climatology curve is not quite correct. Nevertheless, when more data and different data types are used as inputs to PRISM, it should yield improved ionospheric predictions relative to climatology models.

Data-Driven, Physics-Based Models

Physics-based models of the ionosphere have been around for more than 40 years and are very effective for elucidating ionospheric behavior. With this approach, one typically solves continuity, momentum, and energy equations for the ions and electrons taking into account all of the chemical and transport processes thought to be important. The equations are solved numerically as a function of time on a global spatial grid, and the output is three-dimensional distributions of plasma densities, temperatures, and drifts at specified times. If the physics and chemistry in the physics-based ionospheric models are correct, the calculated plasma parameters should describe the real ionosphere. However, stand-alone ionospheric models require magnetospheric and atmospheric inputs, and the accuracy of a model's output depends on the quality of the inputs. The main inputs are 1) global distributions of neutral densities, temperatures, and winds; 2) convection electric fields and particle precipitation at high latitudes; and 3) dynamo electric fields at low latitudes. Unfortunately, the inputs are needed as a function of time, particularly during geomagnetic storms and substorms.

One usually adopts empirical models for the neutral densities, temperatures, and winds if a stand-alone ionosphere model is used because there are insufficient real-time measurements of neutral parameters for assimilation into a data-driven neutral model. However, there are sufficient real-time measurements for assimilation into convection electric field and particle precipitation models, and the resulting time-dependent patterns can then be used to drive ionosphere models or coupled ionosphere–thermosphere models. In one approach, SuperDARN radar measurements are used to obtain time-dependent plasma convection patterns, and auroral images from the POLAR spacecraft are used to deduce the associated electron precipitation patterns.[15] However, the most widely used approach for obtaining real-time plasma convection and electron precipitation patterns is the assimilative mapping of ionospheric electrodynamics (AMIE) procedure.[16] A recent study based on the AMIE procedure will be used to show how data-driven physics-based ionospheric models work.

The AMIE procedure combines a diverse set of real-time measurements and statistical models using four separate least-square fitting algorithms to obtain time-dependent patterns of auroral electron precipitation, convection electric fields, currents, and height-integrated conductances. Recently, the AMIE procedure was used to deduce the ionospheric electrodynamic parameters at high latitudes for the period of 28–29 March 1992.[17,18] For this two-day period, measurements pertaining to the electrodynamic parameters were available from several satellites (IMP-8, DMSP F8-F11, NOAA-12, UARS, and Exos D), a few radars (Sonderstrom incoherent scatter radar, and Wick, Goose Bay, and Halley Bay coherent scatter radars), and 93 magnetometers. The measurements were assimilated via the AMIE procedure, and the result was time-dependent convection and precipitation patterns for both the northern and southern polar regions for the two-day period. As an example of the type of patterns obtained, Fig. 4 shows consecutive plasma convection patterns in the northern hemisphere for the time interval 0810–1030 UT, whereas Fig. 5 shows the corresponding field-aligned current patterns. In Fig. 4, the contour interval is 5 kV, and the cross polar cap potential is given in the upper-right part of each panel. In Fig. 5, the contour interval is 0.2 μA/m^2, starting at $\pm$0.1 μA/m^2. Solid contours show downward currents and dashed contours show upward currents. Note that the upward currents are associated with precipitating auroral electrons. It is apparent that both patterns display appreciable variations during this 2.5-h period.

The time-dependent convection and precipitation patterns obtained from the AMIE procedure were then used to drive the National Center for Atmospheric Research (NCAR) thermosphere–ionosphere general circulation model (TIGCM), and the calculated neutral and plasma parameters were compared with measured parameters. For the two-day period (28–29 March 1992), the TIGCM was driven by 66 northern hemisphere and 53 southern hemisphere AMIE patterns of plasma convection and auroral precipitation. During periods when geomagnetic activity was enhanced, joule heating resulted in decreased O/N_2 ratios in certain regions, and, subsequently, the O/N_2 depletions moved equatorward and typically westward in longitudinal strips. The large-scale O/N_2 depletions lasted about 24 h. These decreased O/N_2 ratios and the enhanced winds that were also generated during enhanced magnetic activity had a significant effect on the ionosphere. Figure 6 shows a comparison of corresponding $N_m F_2$ and $h_m F_2$ calculated by the AMIE-driven TIGCM with ionosonde measurements at four stations (Resolute Bay, Lycksele, Tahiti, and Ouagadougou). The number after the station name is the apex latitude of the station. Vertical lines show local midnight and asterisks are the measurements. The dashed lines are the observed averages between 24 March and 4 April 1992. The solid lines are the TIGCM calculations using time-varying AMIE inputs, whereas the dotted lines correspond to time-averaged AMIE inputs. These comparisons and others at different ionosonde stations indicate that, in general, the TIGCM driven by time-dependent AMIE inputs yields reliable results. However, there are times and locations where the comparisons are not that good. For example, the AMIE-TIGCM simulation underestimated the electron density after midnight by up to a factor of two at midlatitudes, and the calculated $h_m F_2$ was about 35 km lower than observed at midnight. Such discrepancies may simply be related to small errors in where the maximum joule heating occurs, and these small errors can only be resolved by increasing the number of stations that provide measurements for the AMIE data assimilation procedure.

Coupled Physics-Based Models

As noted in the preceding section, a stand-alone ionospheric model needs time-dependent magnetospheric and atmospheric inputs. However, one way to eliminate the need for the inputs is to couple the ionospheric model to physics-based models that describe other spatial domains. Currently, there are coupled global models of the ionosphere–thermosphere, ionosphere–plasmasphere, ionosphere–polar wind, ionosphere–thermosphere–mesosphere, and ionosphere–thermosphere–plasmasphere.[19–23] Also, work has begun on coupling a global ionospheric model to an magnetohydrodynamics (MHD) model of the global magnetosphere.[24] The main advantage of coupled global models is that the coupling processes, time delays, and feedback mechanisms that are inherent in the near-Earth space environment are included in a self-consistent manner. Another advantage is that it is possible to relate disturbances in one

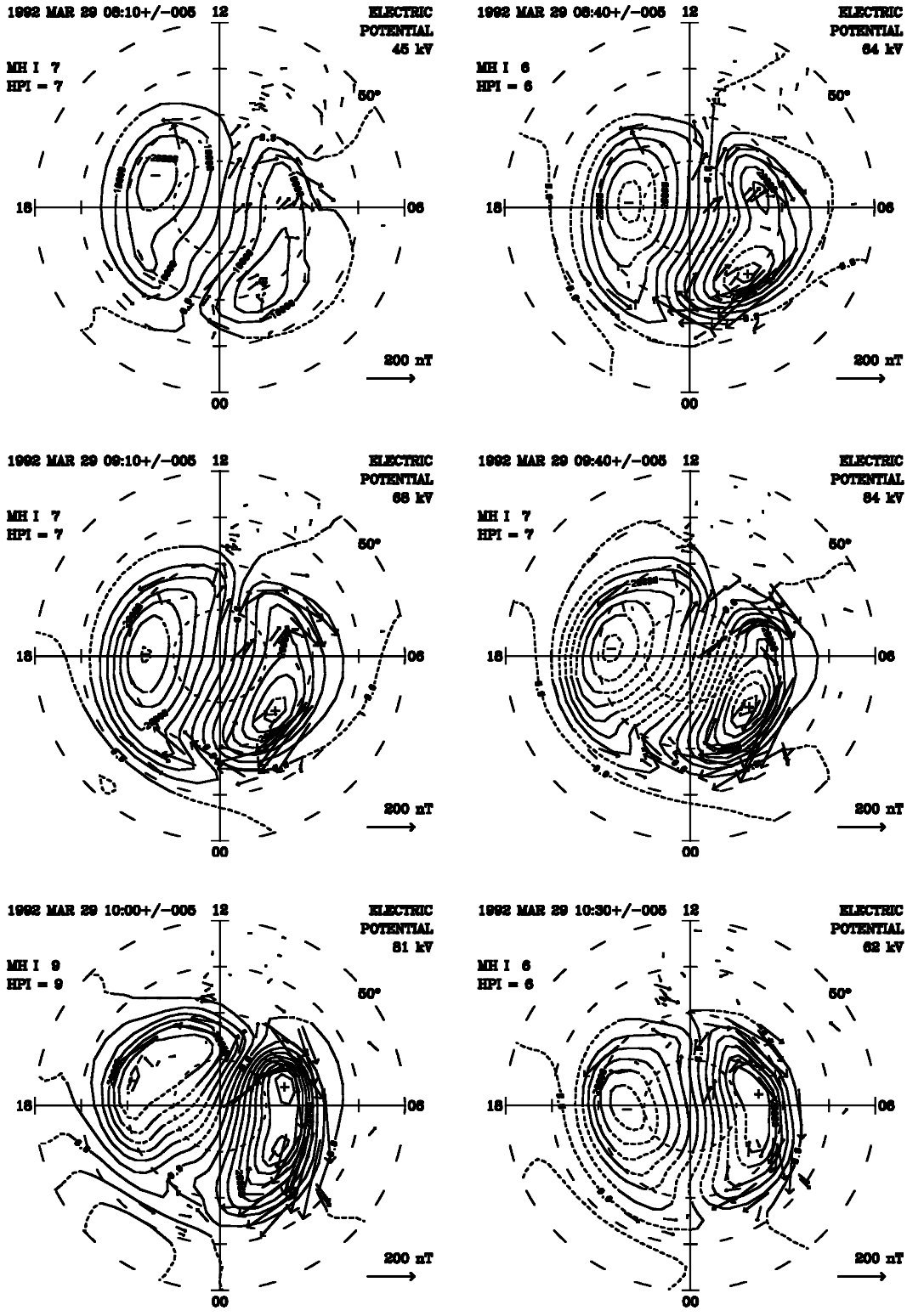

Fig. 4 Consecutive electric potential patterns in the northern hemisphere between 0810 and 1030 UT on 29 March 1992.[18]

domain to causative processes in another domain. On the other hand, a disadvantage is that error propagation from model to model can lead to unreliable quantitative results. In addition, coupled physics-based models tend to require an excessive amount of CPU time.

A model that connects the magnetosphere and ionosphere would be useful for forecasting ionospheric weather because changes in the solar wind measured at the L1 point could be traced to the ionosphere. As a first step in this direction, the Utah State University (USU) model of the global ionosphere[25,26] was used in conjunction with the Naval Research Laboratoy's MHD model of the magnetosphere.[27] The USU ionosphere model is a time-dependent, three-dimensional, multiion model that is global and covers the altitude range from 90 to 1000 km. The model calculates electron and ion densities, temperatures, and drifts via a numerical solution of the appropriate continuity, momentum, and energy equations. From these outputs, height-integrated electrical conductivities can be calculated as a function of time, which are needed by the MHD magnetosphere model. The global magnetosphere model is based

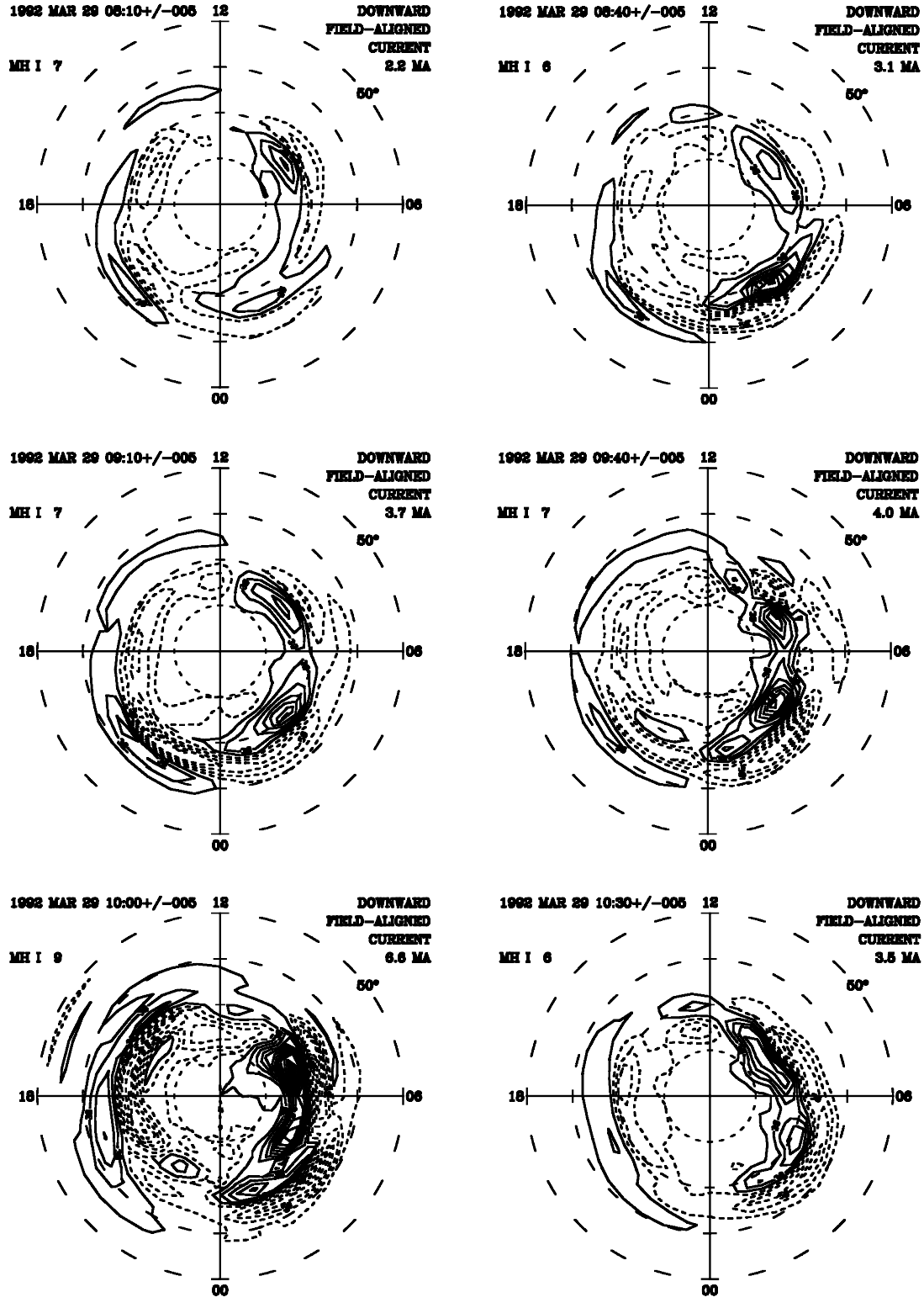

Fig. 5 Field-aligned current patterns that correspond to the electric potential patterns in Fig. 4.[18]

on the ideal MHD equations that describe the interaction of the solar wind with the outer magnetosphere (beyond $3.5R_E$). The MHD model uses a nonorthogonal adapted mesh and a 1-s time step, and it properly accounts for the propagation of fast Alfvén waves on the mesh. The MHD magnetospheric model calculates convection electric field and field-aligned current patterns as a function of time. With the aid of simple algorithms, the field-aligned currents can be converted into electron precipitation patterns. The time-dependent convection and precipitation patterns are needed to drive the ionospheric model.

As a forerunner to a fully coupled magnetosphere–ionosphere model, initial studies were conducted in which the ionosphere and magnetosphere models were run in an iterative manner.[24,28] This initial approach was adopted to determine whether the spatial and temporal steps in the two models were compatible and to identify unexpected coupling problems (Fig. 7). In these initial studies, the MHD magnetosphere model was used to simulate time-dependent convection and precipitation patterns for specific geophysical events, and these patterns were then used to drive the global ionosphere model. These initial studies showed that it was both feasible and

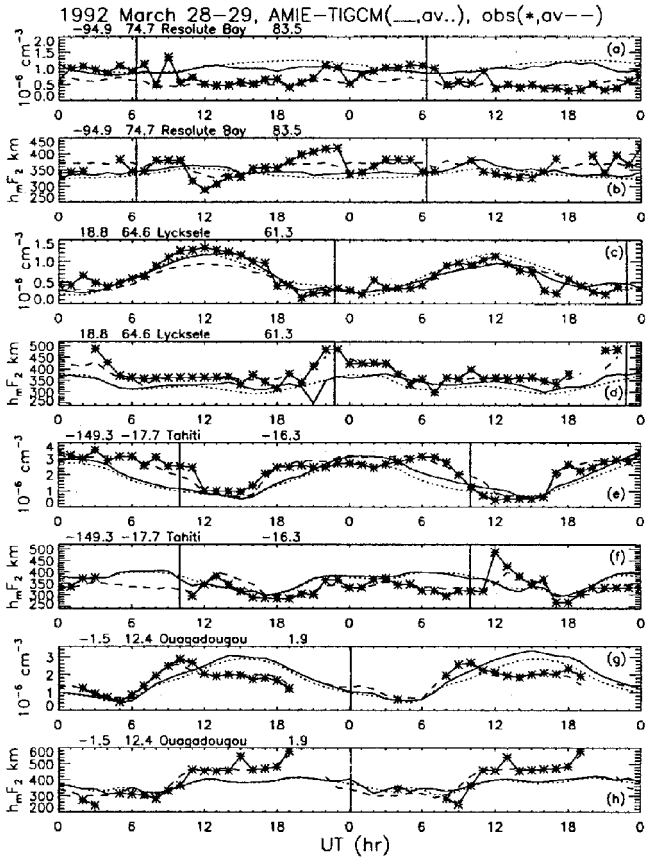

Fig. 6 Ionosonde observations for 28–29 March 1992.[17]

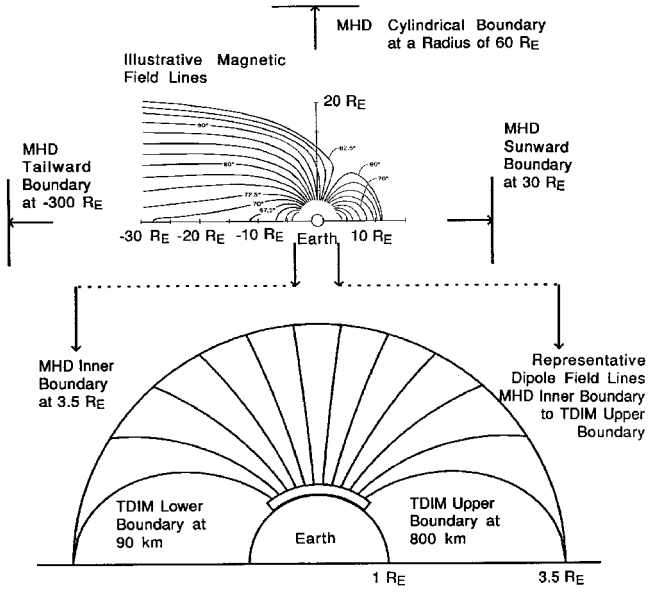

Fig. 7 Schematic diagram showing the interface geometry connected with the time-dependent ionosphere model (TDIM) and the MHD magnetosphere model.[24]

scientifically valuable to couple global models of the magnetosphere and ionosphere.

For one of the geophysical events, solar wind measurements were made as a magnetic cloud passed the Earth. The event occurred on 14 January 1988 and lasted 30 h. During this period, the IMF changed slowly from northward to southward and the B_y component rotated from positive to negative. The event contained a geomagnetic storm, with the growth and expansion phases covering several hours. The measured solar wind parameters were used to drive the MHD model of the magnetosphere, and it produced time-dependent convection and precipitation patterns for the storm period. These patterns, in turn, were used to drive the ionosphere model. Consequently, it was possible to model the ionospheric response to a geomagnetic storm, as predicted by the MHD magnetosphere model. This geomagnetic storm was then simulated again, but for this second simulation, the ionosphere model was driven by time-dependent convection and precipitation patterns obtained from well-known empirical models.[29,30] Finally, the time-dependent electron density distributions obtained from the two ionospheric storm simulations were compared with defense meteorological satellite program (DMSP) satellite measurements at 840 km to determine which of the two simulations was the best. Both simulations successfully predicted the polar hole and the tongue of ionization that were observed at certain times during the storm. However, the MHD-driven ionospheric simulation was clearly superior at all times, as seen in the representative comparison shown in Fig. 8. In Fig. 8, the dials show electron density distributions at 2130 UT. The left dial shows the results for the simulation driven by convection and precipitation patterns calculated with the MHD magnetosphere model. The right dial shows the results when empirical convection[29] and precipitation[30] patterns are used. The bottom diagram shows the comparison of the two simulations with DMSP satellite measurements. On the other hand, both simulations failed to produce the storm enhanced density (SED) region that was observed at certain UTs. The reason for this failure is unclear, but for the MHD-driven simulation it might be due to the lack of feedback between the ionosphere and magnetosphere models.

Tomography

Tomography was first used in an ionospheric application in the late 1980s,[31] although this technique was widely used by the medical community for decades. The main reason why tomography has only recently been used in the ionospheric arena is that ionospheric tomography is more difficult than medical tomography, because the ionosphere evolves with time, whereas a patient is generally motionless during a tomographic scan. Also, for ionospheric tomography, the scanning directions are limited. Nevertheless, to date, both radio and optical tomography have been used in ionospheric applications. With radio tomography, radio transmissions from a low-Earth-orbiting satellite (or satellites) are received along a chain of stations, with the stations typically distributed along a line. The signals received at the stations are used to measure the TEC along the ray paths. Each station records a large number of ray paths as the satellite traverses the station, with the pattern of ray paths taking the form of a partially opened fan. With multiple stations along a line, there are a large number of intersecting ray paths, and the associated TECs are inverted by a mathematical algorithm to obtain a two-dimensonal N_e reconstruction as a function of altitude and distance along the chain. Optical tomography works in a similar way, but instead of TECs, one deals with integrated optical emissions.

At the present time, tomography chains exist in the United States, South America, Europe, Russia, and Asia, and these chains can provide information about ionospheric weather in these local regions.[32–37] Although the chains have only been around for a short time, they already have been successful in reconstructing several different ionospheric density structures, including the main trough, boundary blobs, field-aligned plasma structures, traveling ionospheric disturbances, the Appleton anomaly, and equatorial density depletions (bubbles).

Recently, in association with the combined ionospheric campaign (CIC), tomography was used to elucidate the dynamics of plasma depletions in the low-latitude ionosphere during a period of high geomagnetic activity.[38] The depletions were observed in the Caribbean on 26 June 1998 during the period 0300–0800 UT. Throughout this period, magnetic activity was enhanced, with $K_p > 6$. During the CIC campaign, several instruments/receivers were concentrated in the Caribbean. Slant GPS-TEC data were available from 38 ground stations in the eastern part of the United States and from 6 stations in the Caribbean. In addition, the Arecibo incoherent scatter radar was operating, and data were available from DMSP satellites. These data revealed the presence of a large number of ionospheric depletions, with the depletions ranging from 5 to 30 total electron current unit

(TECU), $10^{16}/m^2$. The depletions detected with the GPS receivers are shown in Fig. 9 for 0300–0800 UT on 26 June 1998. In Fig. 9, the diamonds show GPS stations. The solid circles show observed depletions, with the size of the circle related to the depth of the depletion. The curved lines are the 400-km intersect tracks of the GPS satellites. Note that two distinct latitudinal lines of depletions were detected, one at about 10°N geographic latitude and the other at about 22°N.

In an effort to establish the structure of the ionosphere at the time the depletions were observed, Bust et al.[38] used a three-dimensional variational data assimilation (3 DVAR) tomography algorithm to invert the GPS-TEC and Arecibo data. The 3 DVAR algorithm uses a maximum likelihood statistical minimization technique to reconstruct a three-dimensional N_e distribution.[39] The reconstruction for 0715 UT on 26 June 1998 is shown in Fig. 10, where N_e is shown vs altitude and geographic latitude for a longitude of 276°E. The electron densities are in units of 10^{11} m^{-3}. Three distinct regions are evident: 1) At latitudes below 15 deg, the density is relatively high and structured with a shallow depletion near 10°N latitude. 2) Poleward of 15°N is a narrow deep depletion (near 18°N) and a region consistent with several depletions. 3) Beyond 30°N, the density decreases dramatically and eventually falls to very low values. Note that these reconstructed density features are in good agreement with in situ DMSP satellite measurements.

Bust et al.[38] also presented the tomographic reconstruction vs latitude and longitude by plotting the vertical TEC at each location (Fig. 11). Clearly evident is the sharp boundary at about 30°N latitude. Also evident are numerous enhancements and depletions in the low to middle latitude domain, including the depletion at 18°N latitude and 276°E longitude seen in Fig. 11.

Because of the concentration of numerous instruments and the availability of satellite data, Bust et al.[38] were able to verify that their tomographic reconstructions were basically correct. In general, however, the quality of tomographic reconstructions depends on the geometry of the instrument distribution, the inversion algorithm, transmitter and receiver biases, noise, and multipath effects.[33,40] Nevertheless, the quality of tomographic reconstructions can be very high, and tomography is a powerful tool for elucidating ionospheric weather features.

Data Assimilation Models

Data assimilation models have gained prominence in recent years because of the large number of ionospheric measurement that are becoming available. Within 10 years, it is anticipated that there will be more than 200,000 ionospheric measurements per day from a variety of sources. Figure 12 is a schematic of some of the data sources that are, or will be, available for assimilation into specification and forecast models. The data sources include in situ electron density measurements from DMSP satellites, bottomside electron density profiles from digisondes, line-of-sight TECs between ground stations and the GPS satellites, high-quality TECs between low-altitude satellites with radio beacons and certain chains of stations, occultations between various low-altitude satellites and between low- and high-altitude satellites, and line-of-sight UV emission data, which can be used to infer ionospheric parameters. However, the ingestion of different data types into a real-time data assimilation model can lead to erroneous ionospheric reconstructions if care is not exercised, because all data have limitations. For data assimilation in real time, software must be developed to detect and eliminate bad data, to fill data gaps, and to account for data outages. Also, procedures have to be developed to independently analyze data streams for long-term problems such as changes in biases and instrument degradation. In addition, when dealing with integrated data, such as slant TEC and UV emissions, one must take care that electron density gradients are not smoothed because a knowledge of gradients is critical for certain applications.

A Kalman filter is a powerful way of assimilating data into a time-dependent model.[41–44] The Kalman filter combines measurements from an observing system with the information obtained from an ionospheric model, taking into account the corresponding statistical description of uncertainties. The Kalman filter is a sequential least-squares procedure that finds the best estimate of the state at time t based on all information before this time. Formally, the Kalman filter performs a recursive least-squares inversion of all of the observations, for example, slant TEC, in situ satellite data, etc., for the model variable, for example, N_e, using the dynamic model as a constraint. In practice, a weighted average of the model estimate and the measurements is performed, using the relative accuracy of the two as the weights. The net result is an improved estimate of the model variable, where the improvement is in a statistical sense, that is, it has the least expected error given the measurements, model, and error statistics.

A Kalman filter procedure has been successfully used in combination with slant GPS-TEC data to produce two-dimensional maps of vertical TEC,[42,44] and the results are called global ionospheric maps (GIM). In this work, a relatively simple ionospheric model is used in the Kalman filter, whereby the ionosphere is modeled as a thin shell at 450 km. The slant TEC obtained from about 90 ground stations are converted into vertical TEC using a simple obliquity function, which depends only on the local elevation angles of the GPS satellites relative to the ground-based receivers. Elevation angles above 10 deg are considered. The place where a slant TEC penetrates the thin shell is called a pierce point, and the associated vertical TEC is assigned to that location. In addition to the GPS-TEC measurements, TEC gradient information from climatological ionospheric models (IRI and Bent models) are included in the Kalman filter to help fill gaps in the GPS data coverage.[44] The Kalman filter then simultaneously solves for the two-dimensional vertical TEC map and the satellite and receiver biases at regular time intervals throughout the day.

The use of climatological ionospheric models and the conversion of slant TEC to vertical TEC acts to smooth electron density gradients. Consequently, as noted by the authors,[44] the GIM maps are less reliable at low latitudes and during geomagnetic storms because steep N_e gradients are expected at these locations and times. Nevertheless, as more ground-based GPS-TEC and other data are added to the Kalman filter, the more reliable will be the results. A typical GIM map obtained with the current procedure is shown in Fig. 13. This vertical TEC map is for 1700 UT on 6 July 1998. TEC is shown vs geographic latitude and local time. The dots indicate the locations of the GPS receivers used in the map construction. The most prominent feature seen in the map is the TEC signature of the Appleton anomaly, which is evident past local noon near the magnetic equator. Also evident is the smoothing of gradients, because the two electron density crests tend to be blended into one overall N_e enhancement.

There is a real advantage in using multiple data types in the Kalman filter because the limitations associated with one data type can be overcome with the advantages associated with another data type. Recently, Scherliess (see Ref. 45) constructed a data assimilation model for the global ionosphere that included multiple data types and was based on the Kalman filter procedure. Four different data types were considered, but in this initial application only synthetic (model-generated) data were used. The synthetic data were generated from the USU global ionospheric model, which was driven by empirical inputs for this application. At low and middle latitudes, the important inputs are the neutral wind and the equatorial electric field. The empirical horizontal wind model (HWM) was used to generate the neutral wind field as a function of time,[46] and the Fejer et al.[47] empirical model was used for the equatorial electric field. When these empirical inputs are used, the USU model yields ionospheric climatology that is consistent with the empirical inputs. Nevertheless, this climatology is a reasonably good guess for the state of the ionosphere at any time.

The goal of the Scherliess study was not to model climatology, but to reproduce real-time weather features using measurements and a Kalman filter technique. Consequently, a disturbed ionosphere that represents weather was needed for the numerical experiment. The disturbed ionosphere was obtained by first multiplying the neutral winds obtained from the HWM by 5/3 and the empirical electric fields by 1/2, and then using these adjusted inputs to drive the USU ionosphere model. This second ionospheric model run was assumed to represent weather and was taken to be the truth. The first run (climatology) was taken to be the initial (or best) guess of what the

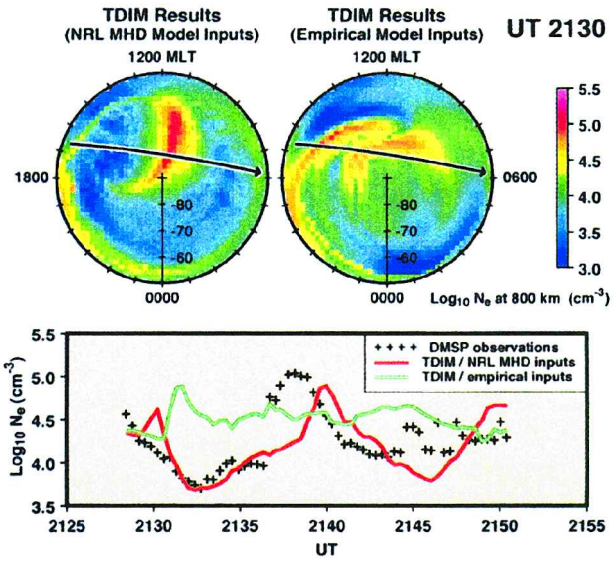

Fig. 8 Comparison of two ionospheric simulations with DMSP satellite observations at 800 km (Ref. 28).

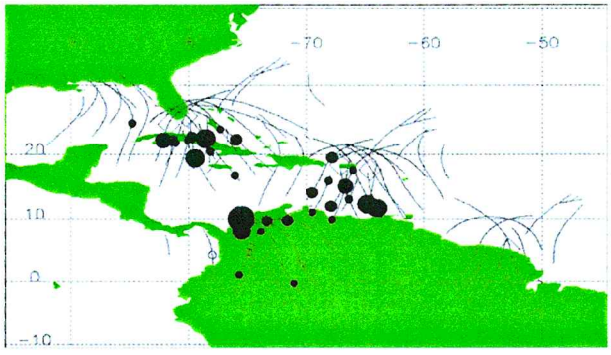

Fig. 9 Ionospheric depletions observed during the period 0300–0800 UT on 26 June 1998.[38]

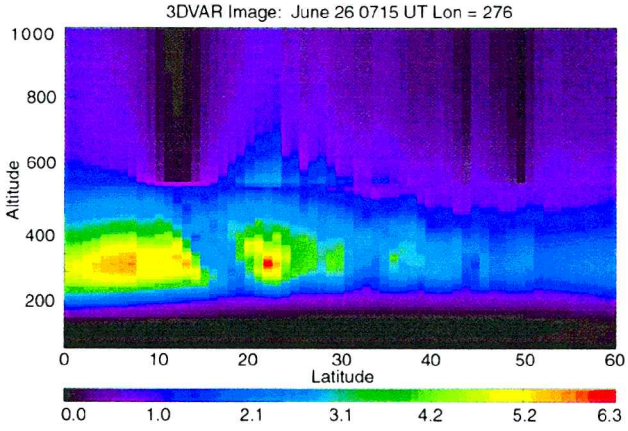

Fig. 10 Electron density reconstruction vs latitude and altitude at 0715 UT on 26 June 1998.[38]

ionosphere looks like at a given time. Figure 14 shows color-coded maps of vertical TEC for the weather (truth) case and the climatology (best guess) case at the start of the numerical experiment (0 UT). The maps are in geographical coordinates from −60° to 60° latitude and 0–24 local time. The top panel shows the synthetic data (truth), the middle panel shows the initial guess, and the bottom panel shows the relative difference between the truth and initial guess. TEC varies from 0 (blue) to 100 (red) TEC units. For the relative difference, blue indicates the initial guess underestimates the truth by 100%, and red indicates an overestimation of 100%. The most prominent feature

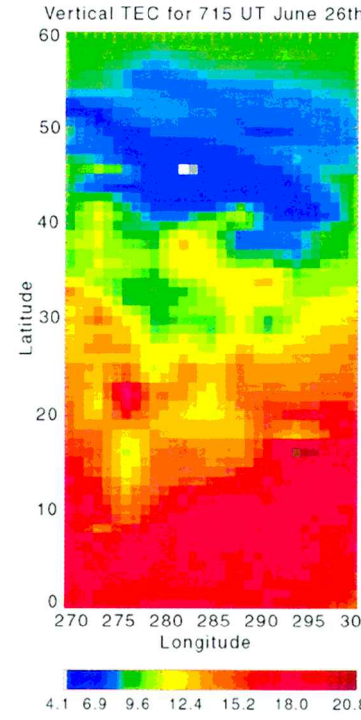

Fig. 11 Vertical TEC obtained by integrating the electron density reconstruction at 0715 UT on 26 June 1998.[38]

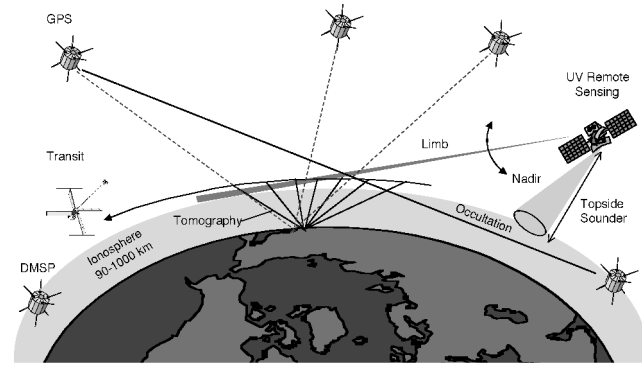

Fig. 12 Schematic diagram showing the different data sources that are available for assimilation into an ionospheric model.

seen in Fig. 14 is the Appleton anomaly, and it also is associated with the largest relative difference between the climatology (initial guess) and the weather (truth) cases.

Four different data types were used in the N_e reconstruction (Fig. 15), including 1) bottomside N_e profiles from 16 digisondes (blue triangles), 2) slant TECs from 23 ground-based GPS receivers (pink plus signs), 3) in situ N_e measurements from two DMSP satellites (pink curves), and 4) TEC occultations from the GPS/MET (meteorology) satellite (yellow curves). The pink curves correspond to 1-h satellite tracks for both of the DMSP satellites. The yellow curve is the corresponding GPS/MET satellite track. The GPS receiver/satellite fields of view for a 1-h period are shown by the blue curves. The instrument configuration is for 0130 UT. Although only synthetic data were used in association with these data sources, the locations of the stations and the measurement geometries were real. The DMSP and GPS/MET satellite orbits that were adopted correspond to the orbits of real satellites. Likewise, the 16 digisondes and the 23 ground-based GPS receivers that were adopted correspond to those that are in the U.S. Air Force network. The synthetic data were generated by probing the three-dimensional, time-dependent N_e distribution for the weather (truth) simulation exactly the way real instruments probe the real ionosphere. For the GPS receivers, slant TECs were generated between 90 and 1000 km and only for elevation angles greater than 30 deg. When the synthetic data were generated, noise was added to each measurement to mimic a real

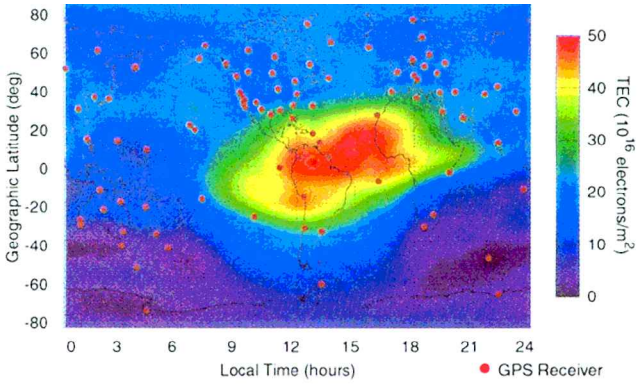

Fig. 13 Vertical TEC map for 1700 UT on 6 July 1998 as obtained from the GIM procedure.[44]

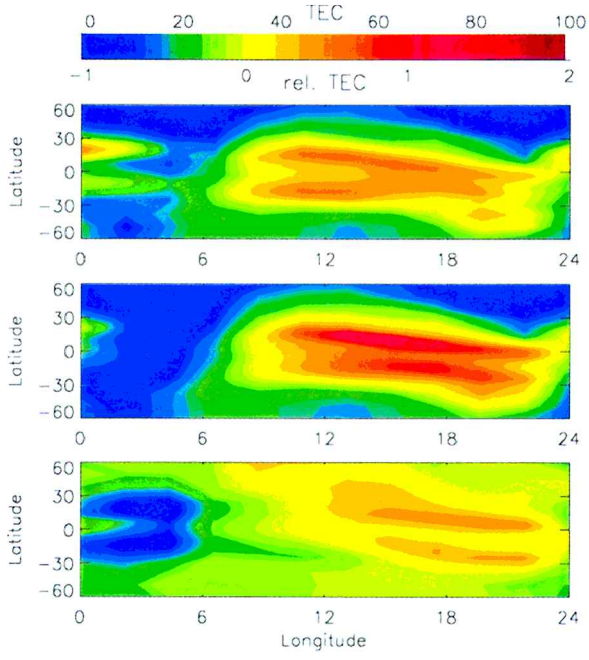

Fig. 14 Maps of vertical TEC in the low–middle latitude domain.[45]

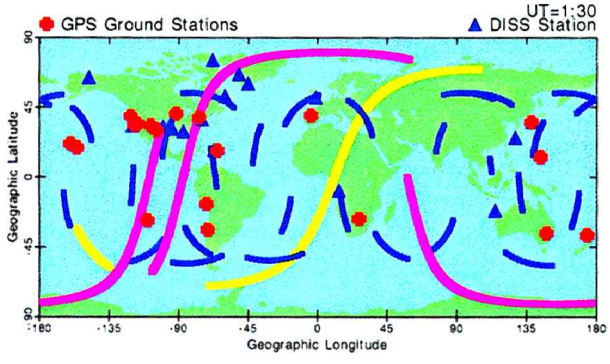

Fig. 15 Simulated data sources.[45]

measurement. The level of noise for the synthetic TEC measurements was 5 TECU, and all other simulated measurements were assumed to have a 10% uncertainty.

The Kalman filter data reconstruction procedure was implemented as follows. The N_e distribution obtained from the climatology run at 0 UT was taken to be the initial N_e distribution at the start of the N_e reconstruction. This N_e distribution was basically the best guess for the ionospheric state before reconstruction. Then, the evolving weather simulation was probed every hour to

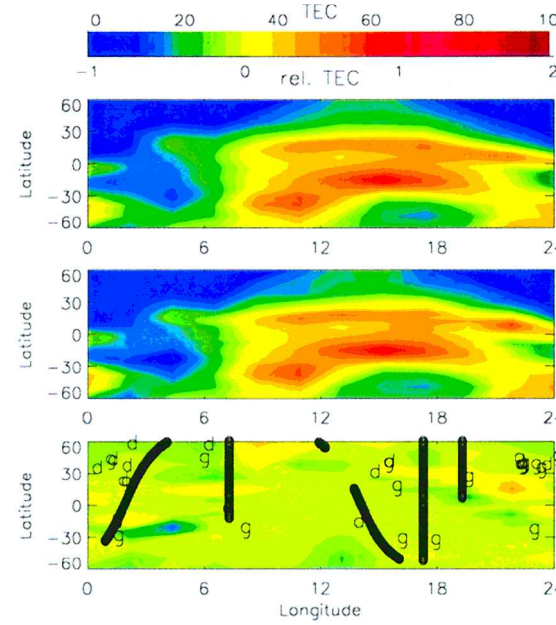

Fig. 16 Kalman filter reconstruction of vertical TEC.[45]

obtain the synthetic measurements (with noise) for the four different data types, as described earlier. These synthetic measurements were subsequently input into the Kalman filter every hour, and a simple Gauss–Markov process was used to advance time in the filter. The Kalman filter started from the climatology N_e distribution, and as time advanced, the Kalman filter produced a three-dimensional N_e distribution that got closer and closer to the time-varying N_e distribution associated with the weather simulation. Basically, the Kalman filter was able to lock on to the evolving weather N_e distribution with just hourly measurements from the four different data types. Figure 16 shows a comparison of the Kalman filter reconstruction of vertical TEC and the weather (truth) simulation at 0600 UT. The top panel shows the TEC map from the weather simulation (truth), the middle panel shows the Kalman filter reconstruction using the simulated measurements, and the bottom panel shows the TEC difference between the truth and the reconstruction. In the bottom panel, d shows the locations of the digisondes, g shows the locations of the ground-based GPS receivers, the vertical lines show the DMSP satellite tracks for a 1-h period, and the curved solid line shows the GPS/MET satellite track for a 1-h period. It is apparent that the Kalman filter was successful in capturing the ionospheric TEC distribution, and at 0600 UT, the difference between the truth and reconstructed TEC is typically much less than 1 TECU.

Conclusions

Ionospheric weather is having an ever increasing effect on both military and civilian systems and, as a consequence, a large effort is being devoted to developing specification and forecast models. Virtually all model types are currently being used to both specify and forecast ionospheric disturbances, including empirical, parameterized, numerical, tomographic, and data assimilation models. In recent years, tomographic and physics-based data assimilation models have gained prominence because of the large data sets that will be available in the not too distant future. During the next decade, it is anticipated that there will be 200,000 or more ionospheric measurements per day from a variety of data sources. With such a large number of measurements, tomographic and physics-based assimilation models are very attractive. Currently, there are well over 100 ionospheric models of various types, and the interested reader can obtain additional information about some of the model types from relatively recent review articles or books, including empirical, numerical, and tomographic models.[1,9,21,32]

With the advent of more than 200,000 ionospheric measurements per day, time-dependent, global, ionospheric reconstructions will be

available on a continuous basis in the near future, and this will have a major impact on ionospheric physics. When able to reconstruct the detailed ionospheric behavior for a wide range of geophysical conditions, it should be possible to resolve a host of long-standing basic science issues, including 1) the onset of equatorial spread F, 2) the morphology of equatorial plasma bubbles, 3) plasmaspheric refilling rates after geomagnetic storms and substorms, 4) the morphology of the midlatitude trough, 5) the plasma and neutral gas evolution during storms, 6) the plasma convection pattern for northward IMF, and many more. Consequently, a major advance in ionospheric physics can be anticipated during the next decade.

References

[1]Schunk, R. W., and Nagy, A. F., *Ionospheres*, Cambridge Univ. Press, Cambridge, England, U.K., 2000, pp. 1–554.

[2]Kleusberg, A., "The Global Positioning System and Ionospheric Conditions," *Solar-Terrestrial Predictions*, Vol. 4, National Oceanic and Atmospheric Administration, Boulder, CO, l992, pp. 142–146.

[3]Shapka, R., "Geomagnetic Effects on Modern Pipeline Systems," *Solar-Terrestrial Predictions*, Vol. 4, National Oceanic and Atmospheric Administration, Boulder, CO, 1992, pp. 163–170.

[4]Cliffswallow, W., and Hirman, J. W., "U.S. Space Weather Real-Time Observing and Forecasting Capabilities," *Solar-Terrestrial Predictions*, Vol. 4, National Oceanic and Atmospheric Administration, Boulder, CO, 1992, pp. 185–198.

[5]El-Arini, M. B., Poor, W., Lejeune, R., Conker, R., Fernow, J. P., and Markin, K., "An Introduction to WAAS and Its Predicted Performance," edited by J. M. Goodman, *Proceedings of 1999 Ionospheric Effects Symposium*, JMG Associates, Alexandria, VA, 1999, pp. 211–220.

[6]Tribble, A. C., *The Space Environment—Implications for Spacecraft Design*, Princeton Univ. Press, Princeton, NJ, 1995.

[7]Hastings, D., and Garrett, H., *Spacecraft Environment Interactions*, Cambridge Univ. Press, Cambridge, England, U.K., 1996.

[8]Bent, R. B., Llewellyn, S. K., and Schmid, P. E., "Ionospheric Refraction Corrections in Satellite Tracking," *Space Research*, Vol. 12, 1992, No. 11, pp. 1186–1194.

[9]Bilitza, D., Rawer, K., Bossy, L., and Gulyaeva, T., "International Reference Ionosphere—Past, Present, and Future, I, Electron Density," *Advances in Space Research*, Vol. 13, No. 1, 1993, pp. 3–13.

[10]Szuszczewicz, E. P., "The Modeling, Measurement and Predictability of the Global-Scale Ionosphere," *Proceedings of the Solar Terrestrial Predictions Workshop*, edited by P. J. Wilkerson, Leura, Australia, 1989, pp. 1–31.

[11]Daniell, R. E., Brown, L. D., Anderson, D. N., Fox, M. W., Doherty, P. H., Decker, D. T., Sojka, J. J., and Schunk, R. W., "Parameterized Ionospheric Model: A Global Ionospheric Parameterization Based on First Principles Models," *Radio Science*, Vol. 30, No. 7, 1995, pp. 1499–1510.

[12]Decker, D. T., Wise, J. O., Borer, W. S., Daniell, R. E., and Doherty, P. H., "Validation of PRISM: Real Time Specification," *Proceedings of 1999 Ionospheric Effects Symposium*, edited by J. M. Goodman, JMG Associates, Alexandria, VA, 1999, pp. 340–347.

[13]Bishop, G., Daniell, R., Bullett, T., Rao, S., Mazzella, A., and Denny, T., "An Application of PRISM to Regional Ionospheric Specifications," *Proceedings of 1999 Ionospheric Effects Symposium*, edited by J. M. Goodman, JMG Associates, Alexandria, VA, 1999, pp. 352–359.

[14]Doherty, P. H., Decker, D. T., Sultan, P. J., Rich, F. J., Borer, W. S., and Daniell, R. E., "Validation of PRISM: The Climatology," *Proceedings of 1999 Ionospheric Effects Symposium*, edited by J. M. Goodman, JMG Associates, Alexandria, VA, 1999, pp. 330–339.

[15]Shepherd, S. G., and Ruohoniemi, J. M., "Electrostatic Potential Patterns in the High-Latitude Ionosphere Constrained by SuperDARN Measurements," *Journal of Geophysical Research*, Vol. 105, No. A10, 2000, pp. 23005–23014.

[16]Richmond, A. D., "Assimilative Mapping of Ionospheric Electrodynamics," *Advances in Space Research*, Vol. 12, No. 6, 1992, p. 59.

[17]Emery, B. A., Lu, G., Szuszczewicz, E. P., Richmond, A. D., Roble, R. G., Richards, P. G., Miller, K. L., Niciejewski, R., Evans, D. J., Rich, F., Denig, W. F., Chenette, D. L., Wilkinson, P., Pulinets, S., Loughlin, F. O., Hanbaba, R., Abdu, M., Jiao, P., Igarashi, K., and Reddy, B. M., "Assimilative Mapping of Ionospheric Electrodynamics in the Thermosphere-Ionosphere General Circulation Model Comparisons with Global Ionospheric and Thermospheric Observations During the GEM/SUNDIAL Period of March 28–29, 1992," *Journal of Geophysical Research*, Vol. 101, No. A12, 1996, pp. 26681–26696.

[18]Lu, G., Emery, B. A., Rodger, A. J., Lester, M., Taylor, J. R., Evans, D. S., Ruohoniemi, J. M., Denig, W. F., de la Beaujardiere, O., Frahm, R. A., Winningham, J. D., and Chenette, D. L., "High-Latitude Ionospheric Electrodynamics as Determined by the Assimilative Mapping of Ionospheric Electrodynamics Procedure for the Conjunctive SUNDIAL/ATLAS 1/GEM Period of March 28–29, 1992," *Journal of Geophysical Research*, Vol. 101, No. A12, 1996, pp. 26697–26718.

[19]Fuller-Rowell, T. J., Codrescu, M. V., Moffett, R. J., and Quegan, S., "Response of the Thermosphere and Ionosphere to Geomagnetic Storms," *Journal of Geophysical Research*, Vol. 99, No. A3, 1994, pp. 3893–3914.

[20]Roble, R. G., and Dickinson, R. E., "How will Changes in Carbon Dioxide and Methane Modify the Mean Structure of the Mesosphere and Thermosphere?," *Geophysical Research Letters*, Vol. 16, No. 12, 1989, pp. 1441–1444.

[21]Millward, G. H., Moffett, R. J., Quegan, S., and Fuller-Rowell, T. J., "A Coupled Thermosphere-Ionosphere-Plasmasphere Model (CTIP)," *STEP Handbook of Ionospheric Models*, edited by R. W. Schunk, Utah State Univ. Press, Logan, UT, 1996, pp. 239–279.

[22]Richards, P. G., and Torr, D. G., "The Field Line Interhemispheric Plasma Model," *STEP Handbook of Ionospheric Models*, edited by R. W. Schunk, Utah State Univ. Press, Logan, UT, 1996, pp. 207–216.

[23]Schunk, R. W., and Sojka, J. J., "The Global Ionosphere-Polar Wind System During Changing Magnetic Activity," *Journal of Geophysical Research*, Vol. 102, No. A6, 1997, pp. 11625–11651.

[24]Sojka, J. J., Schunk, R. W., Bowline, M. D., Chen, J., Slinker, S., and Fedder, J. A., "Driving a Physical Ionospheric Model with a Magnetospheric MHD Model," *Journal of Geophysical Research*, Vol. 102, No. A10, 1997, pp. 22209–22220.

[25]Schunk, R. W., "A Mathematical Model of the Middle and High Latitude Ionosphere," *Pure and Applied Geophysics*, Vol. 127, No. 2/3, 1988, pp. 255–303.

[26]Sojka, J. J., "Global Scale, Physical Models of the F Region Ionosphere," *Reviews of Geophysics*, Vol. 27, No. 3, 1989, pp. 371–403.

[27]Fedder, J. A., Slinker, S. P., Lyon, J. G., and Elphinstone, R. D., "Global Numerical Simulation of the Growth Phase and the Expansion Onset for a Substorm Observed by Viking," *Journal of Geophysical Research*, Vol. 100, No. A10, 1995, pp. 19083–19093.

[28]Sojka, J. J., Schunk, R. W., Bowline, M. D., Chen, J., Slinker, S., Fedder, J., and Sultan, P. J., "Ionospheric Storm Simulations Driven by Magnetospheric MHD and Empirical Models; With Data Comparisons," *Journal of Geophysical Research*, Vol. 103, No. A10, 1998, pp. 20669–20684.

[29]Heppner, J. P, and Maynard, N. C., "Empirical High-Latitude Electric Field Models," *Journal of Geophysical Research*, Vol. 92, No. A5, 1987, pp. 4467–4489.

[30]Hardy, D. A., Gussenhoven, M. S., Raistrick, R., and McNeil, W. J., "Statistical and Functional Representations of the Pattern of Auroral Energy Flux, Number Flux, and Conductivity," *Journal of Geophysical Research*, Vol. 92, No. A11, 1987, pp. 12275–12294.

[31]Austen, J. R., Franke, S. J., and Liu, C. H., "Ionospheric Imaging Using Computerized Tomography," *Radio Science*, Vol. 23, No. 2, 1988, pp. 299–307.

[32]Leitinger, R., "Tomography," *Modern Ionospheric Science*, edited by H. Kohl, R. Rüster, and K. Schlegel, European Geophysical Society, Katenburg-Lindall, Germany, 1996, pp. 346–370.

[33]Andreeva, E. S., Franke, S. J., Yeh, K. C., Kunitsyn, V. E., and Nesterov, I. A., "Experiments, Data Processing and Results in Ionospheric Tomography: General Requirements, Restrictions and Possibilities," *Proceedings of 1999 Ionospheric Effects Symposium*, edited by J. M. Goodman, JMG Associates, Alexandria, VA, 1999, pp. 90–97.

[34]Andreeva, E. S., Franke, S. J., Yeh, K. C., and Kunitsyn, V. E., "Some Features of the Equatorial Anomaly Revealed by Ionospheric Tomography," *Geophysical Research Letters*, Vol. 27, No. 16, 2000, pp. 2465–2468.

[35]Bust, G. S., and Coco, D., "CIT Analysis of the Combined Ionospheric Campaigns (CIC)," *Proceedings of 1999 Ionospheric Effects Symposium*, edited by J. M. Goodman, JMG Associates, Alexandria, VA, 1999, pp. 508–518.

[36]Kersley, L., "The Application of Radio Tomography to Ionospheric Mapping and High-Latitude Geophysics," *Proceedings of 1999 Ionospheric Effects Symposium*, edited by J. M. Goodman, JMG Associates, Alexandria, VA, 1999, pp. 58–65.

[37]Kunitsyn, V. E., Razinkov, O. G., Zakharov, V. I., Andreeva, E. S., and Yeh, K. C., "Possibilities of Regional Monitoring of the Ionosphere by Radio Tomography Using Low- and High-Orbit Systems," *Proceedings of 1999 Ionospheric Effects Symposium*, edited by J. M. Goodman, JMG Associates, Alexandria, VA, 1999, pp. 98–105.

[38]Bust, G. S., Coco, D., and Makela, J. J., "Combined Ionospheric Campaign 1: Ionospheric Tomography and GPS Total Electron Count (TEC) Depletions," *Geophysical Research Letters*, Vol. 27, No. 18, 2000, pp. 2849–2852.

[39]Daley, R., and Barker, E., "The NRL 3DVAR Source Book," Naval Research Lab., Monterey, CA, 1998.

[40]Bavel, G. V., Brown, A., and Ganguly, S., "Ionospheric Tomography: Issues, Sensitivities, Uniqueness," *Proceeding of 1999 Ionospheric Effects Symposium*, edited by J. M. Goodman, JMG Associates, Alexandria, VA, 1999, pp. 78–89.

[41]Gelb, A., *Applied Optimal Estimation*, MIT Press, Cambridge, MA, 1974, pp. 1–374.

[42]Wilson, B. D., Mannucci, A. J., and Edwards, C. D., "Subdaily Northern Hemisphere Ionospheric Maps Using an Extensive Network of GPS Receivers," *Radio Science*, Vol. 30, No. 3, 1995, pp. 639–648.

[43]Howe, B. M., Runciman, K., and Secan, J. A., "Tomography of the Ionosphere: Four-Dimensional Simulations," *Radio Science*, Vol. 33, No. 1, 1998, pp. 109–128.

[44]Iijima, B. A., Harris, I. L., Ho, C. M., Lindqwister, U. J., Mannucci, A. J., Pi, X., Reyes, M. J., Sparks, L. C., and Wilson, B. D., "Automated Daily Process for Global Ionospheric Total Electron Content Maps and Satellite Ocean Altimeter Ionospheric Calibration Based on Global Positioning System Data," *Journal of Atmospheric and Solar-Terrestrial Physics*, Vol. 61, No. 16, 1999, pp. 1205–1218.

[45]Schunk, R. W., Scherliess, L., and Sojka, J. J., "Recent Approaches to Modeling Ionospheric Weather," *Advances in Space Research* (to be published).

[46]Hedin, A. E., Spencer, N. W., and Killeen, T. L., "Empirical Global Model of Upper Thermosphere Winds Based on Atmosphere and Dynamics Explorer Satellite Data," *Journal of Geophysical Research*, Vol. 93, No. A9, 1988, p. 9959.

[47]Fejer, B. G., de Paula, E. R., Heelis, R. A., and Hanson, W. B., "Global Equatorial Ionospheric Vertical Plasma Drifts Measured by the AE-E Satellite," *Journal of Geophysical Research*, Vol. 100, No. A4, 1995, p. 5769.

A. C. Tribble
Associate Editor